Physical constraints on geologic CO_2 sequestration in low-volume basalt formations

Ryan M. Pollyea[1,†], Jerry P. Fairley[2], Robert K. Podgorney[3], and Travis L. Mcling[4]
[1]*Department of Geology & Environmental Geosciences, Northern Illinois University, DeKalb, Illinois 60115, USA*
[2]*Department of Geological Sciences, University of Idaho, Moscow, Idaho 83844, USA*
[3]*Energy Resource Recovery and Sustainability, Idaho National Laboratory, Idaho Falls, Idaho 83415, USA*
[4]*Center for Advanced Energy Studies, Idaho National Laboratory, Idaho Falls, Idaho 83415, USA*

ABSTRACT

Deep basalt formations within large igneous provinces have been proposed as target reservoirs for carbon capture and sequestration on the basis of favorable CO_2-water-rock reaction kinetics that suggest carbonate mineralization rates on the order of 10^2–10^3 d. Although these results are encouraging, there exists much uncertainty surrounding the influence of fracture-controlled reservoir heterogeneity on commercial-scale CO_2 injections in basalt formations. This work investigates the physical response of a low-volume basalt reservoir to commercial-scale CO_2 injections using a Monte Carlo numerical modeling experiment such that model variability is solely a function of spatially distributed reservoir heterogeneity. Fifty equally probable reservoirs are simulated using properties inferred from the deep eastern Snake River Plain aquifer in southeast Idaho, and CO_2 injections are modeled within each reservoir for 20 yr at a constant mass rate of 21.6 kg s^{-1}. Results from this work suggest that (1) formation injectivity is generally favorable, although injection pressures in excess of the fracture gradient were observed in 4% of the simulations; (2) for an extensional stress regime (as exists within the eastern Snake River Plain), shear failure is theoretically possible for optimally oriented fractures if $S_h \leq 0.70S_V$; and (3) low-volume basalt reservoirs exhibit sufficient CO_2 confinement potential over a 20 yr injection program to accommodate mineral trapping rates suggested in the literature.

INTRODUCTION

In 2012, global CO_2 emissions from fossil fuel combustion increased 1.4% to 31.6 Gt (a record high), and in May 2013, average daily atmospheric CO_2 concentrations exceeded 400 ppm for the first time since such measurements have been recorded (IEA, 2013). Several technology-based and policy-driven strategies have been proposed for stabilizing the global CO_2 emissions, one of which is carbon capture and sequestration (CCS) (Pacala and Socolow, 2004). The premise underlying CCS technology is that point-source CO_2 can be captured at industrial operations and pumped into deep geologic formations for permanent disposal, thus preventing atmospheric release. Four trapping mechanisms have been identified for CO_2 disposal in geologic formations: (1) physical trapping beneath a low-permeability cap rock seal, (2) residual saturation trapping of free-phase CO_2 in isolated pore space, (3) solubility trapping of CO_2 dissolved in the aqueous phase, and (4) mineralization by geochemical water-CO_2-rock interactions, resulting in permanently trapped carbonate precipitates (Matter and Kelemen, 2009). The traditional geologic settings for CCS reservoirs are sedimentary basins with low-permeability cap rock seals and depleted oil fields, where the occurrence of hydrocarbon resources indicates the presence of naturally occurring physical trapping mechanisms (Orr, 2009).

Recently, however, a growing body of evidence suggests that large igneous provinces hosting deep basalt reservoirs (>800 m) may be attractive targets for CO_2 disposal on the basis of rapid mineralization reactions (McGrail et al., 2006). Investigation of large igneous provinces for CCS targets is motivated to a large extent by the storage potential within both onshore and offshore basalt formations. For example, the Deccan Traps in central and western India have an estimated storage capacity of 150 Gt CO_2 (Jayaraman, 2007). Similarly, the storage capacity of the Columbia River Basalt Group in the northwestern United States has been estimated to be on the order of 100 Gt CO_2 (McGrail et al., 2006), and offshore basalt formations within the Juan de Fuca plate and Central Atlantic magmatic province hold potential for CO_2 disposal on comparable scales (Goldberg et al., 2008, 2010).

Mineralization reactions for geologic carbon sequestration in basalt reservoirs have been investigated theoretically on the basis of kinetic rate laws (Alexander et al., 2007), and in the laboratory using both grain-scale (McGrail et al., 2006) and core-scale experiments (Schaef et al., 2011). The work by Schaef et al. (2011) has shown that CO_2, dissolved in either the aqueous phase or a water-rich supercritical phase, produces carbonate precipitates when exposed to basalt samples under temperature and pressure conditions representative of reservoir depth for a period of 180 d. Significantly, this work showed increasing mineralization rates with increasing temperature and pressure, suggesting that deep basalt reservoirs with elevated thermal gradients may be ideal targets for CCS implementation; moreover, natural analogs for this process were identified by Kelley et al. (2001) in a Mid-Atlantic Ridge hydrothermal vent field composed of ultramafic peridotite.

Despite the mounting evidence suggesting that mineral trapping will play a significant role in basalt-hosted CO_2 sequestration reservoirs, many questions remain about the feasibility of industrial-scale implementation. For example, basalt-flow morphology is characterized by dense, interconnected fracture networks that provide both CO_2 storage capacity and potential escape pathways. This implies that physical trapping, solubility trapping, and residual saturation trapping will be necessary to hold sequestered CO_2 within the target reservoir over time scales sufficient for mineralization reactions to proceed. Although the influence of fracture heterogeneity on site-scale CCS in basalt reservoirs has received little attention in the literature, recent work by Pollyea and Fairley (2012) shows that the spatial distribution of fracture-controlled reservoir heterogeneity exerts significant control

†E-mail: rpollyea@niu.edu

GSA Bulletin; March/April 2014; v. 126; no. 3/4; p. 344–351; doi:10.1130/B30874.1; 5 figures; 3 tables; Published online 7 January 2014.

on the rate of injection pressure accumulation. Unfortunately, these results were inconclusive with respect to the CO_2 confinement potential in basalt reservoirs over the 10 yr simulation injection period, and the two-dimensional geometry their model did not address the influence of injection pressure on the geomechanical state of the target reservoir. In the present work, we extend the efforts of Pollyea and Fairley (2012) by developing three-dimensional stochastic representations of layered, low-volume basalt reservoirs with characteristics inferred from basalt exposures within the eastern Snake River Plain, Idaho. We simulated CO_2 injections for 20 yr at a constant mass rate of 21.6 kg s^{-1} in 50 equally probable synthetic basalt reservoirs. In this Monte Carlo approach, model variability is solely a function of the spatially distributed fracture heterogeneity, and modeling results are evaluated across 50 individual simulations to investigate (1) the likelihood of exceeding the fracture gradient at injection depth, (2) potential for shear failure of optimally aligned faults or fractures, and (3) confinement potential in the absence of mineralization reactions after a 20 yr injection program.

MODEL DESCRIPTION

Low-volume basalt flows typical of the eastern Snake River Plain are characterized geometrically by a length:width:thickness aspect ratio 30:10:1, respectively, with length scales on the order of 10^1–10^3 m (Welhan et al., 1997, 2002b). Figure 1A presents a cross-sectional image of two adjacent basalt flows observed in outcrop at the Box Canyon field site, which is located within the eastern Snake River Plain ~8 km southeast of Arco, Idaho. In the model presented here, a synthetic assemblage of low-volume basalt flows (Fig. 1B) is simulated as a bimodal stochastic continuum using reservoir properties inferred from previous investigations on the eastern Snake River Plain, and described by Pollyea and Fairley (2012). This representation simplifies the hydrogeologic reservoir properties into (1) high-permeability (*k*) units composed of densely fractured upper colonnades and rubbly flow margins and (2) low-*k* flow interiors. The hydrogeologic properties are presented in Table 1. Fifty equally probable, three-dimensional synthetic reservoirs were generated using a sequential indicator simulation (Deutsch, 2002) such that the spatial distribution of fracture-controlled reservoir heterogeneity is constrained by the model semivariogram and probability distribution function of fracture distributions in

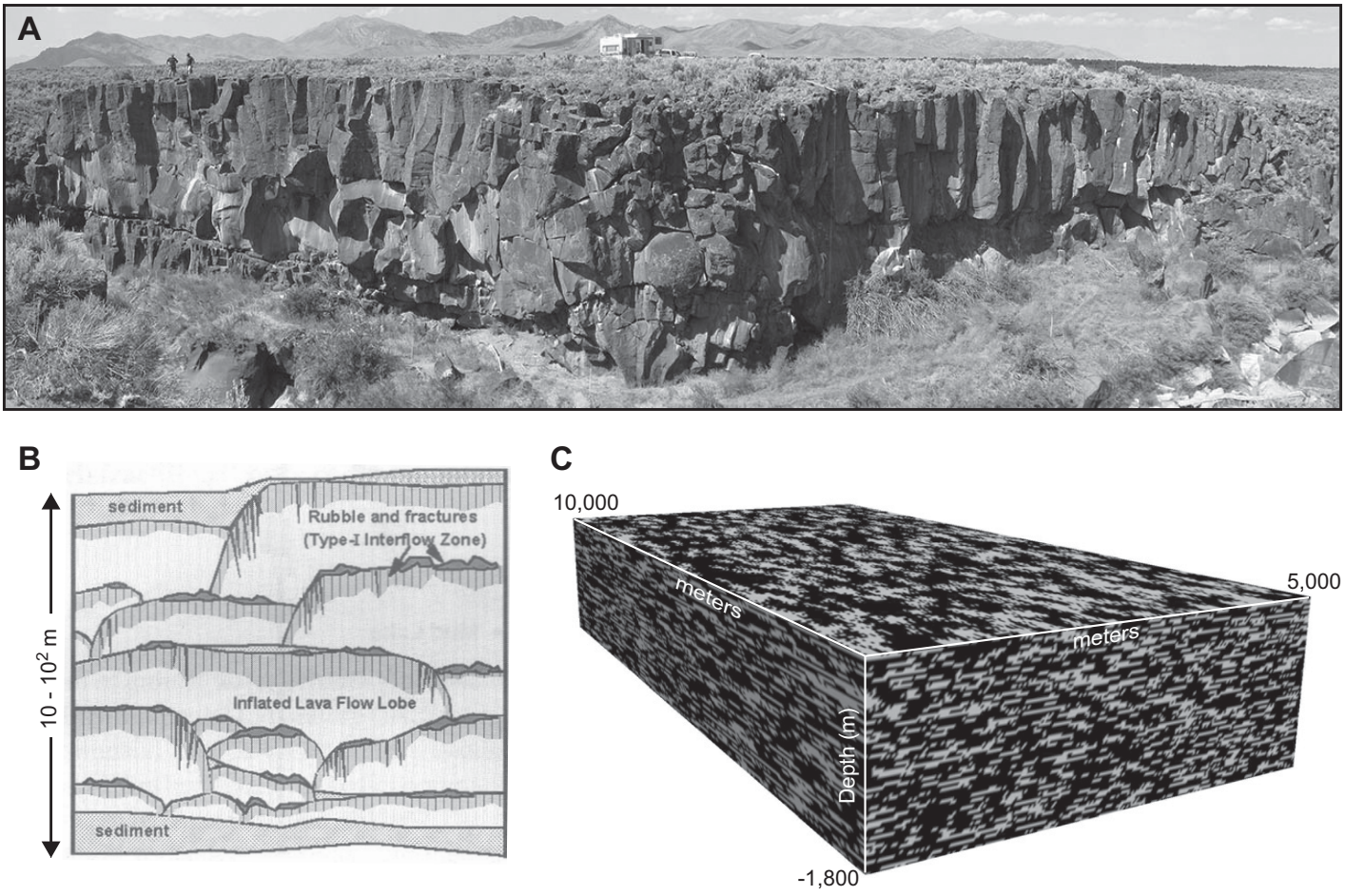

Figure 1. (A) Digital image of adjacent low-volume basalt flows viewed in cross section at an outcrop within the Box Canyon field site, which is located ~8 km southeast of Arco, Idaho. (B) Conceptual model of the eastern Snake River Plain by Welhan et al. (2002c, their fig. 2A) depicting a layered assemblage of low-volume basalt flows. (C) Example of one bimodal synthetic reservoir developed for this work. High-permeability rubble zones and interconnected upper colonnades are identified with gray shading; low-permeability flow interiors are denoted with black shading. Each reservoir contains 2,880,000 grid blocks with individual grid-block geometry of 25 m × 50 m × 25 m (width by length by height, respectively).

TABLE 1. RESERVOIR PROPERTIES

	Flow interior	Rubble zone
ρ_r	2650	2650
ϕ	0.125	0.125
k_x	3.40E–15	1.77E–14
k_y	3.40E–15	1.77E–14
k_z	7.06E–16	1.77E–14

Note: ρ_r—dry density of basalt (kg m^{-3}); ϕ—porosity (–); k—permeability (m^2), where subscript denotes direction; permeability data are from Pollyea and Fairley (2012).

TABLE 2. MODEL SEMIVARIOGRAM PARAMETERS

Direction	Model type	Sill	Range (m)
Minimum horizontal	Nugget	0.30	—
	Exponential	0.15	1.5
	Exponential	0.55	38.0
Maximum horizontal	Nugget	0.30	—
	Exponential	0.15	1.5
	Exponential	0.55	107.0*
Vertical	Nugget	0.30	—
	Exponential	0.15	1.5
	Exponential	0.55	10.0

*From Welhan et al. (2002a, their Fig. 8b).

outcrop. Across the ensemble of 50 reservoir simulations, the probability distribution for each subdomain is 0.31 for the high-*k* unit (densely fractured upper colonnades and rubbly flow margins) and 0.69 for the low-*k* unit (basalt-flow interiors). For the two-dimensional, anisotropic semivariogram model describing the minimum horizontal and vertical fracture correlation, field data were acquired using terrestrial light detection and ranging (LiDAR) by scanning analog outcrop basalt exposures at the Box Canyon field site in southeast Idaho; the field methods are presented in Pollyea and Fairley (2011), and the semivariogram analysis is described in Pollyea and Fairley (2012). In extending the model presented by Pollyea and Fairley (2012) into three dimensions, we augmented the two-dimensional anisotropic semivariogram model by adding a basalt-flow lengthwise correlation structure for the high-*k* facies in the horizontal plane of simulated basalt flows. This component of the anisotropic semivariogram correlation model is based on spatial analysis of hydraulic conductivity data from pumping tests at the Idaho National Laboratory's Test Area North (Welhan et al., 2002a, their fig. 8b), and it is assumed here to represent the axis of maximum horizontal spatial correlation with an effective range parameter of 107 m. The three-dimensional anisotropic semivariogram model for the high-permeability units is presented in Table 2.

Each reservoir is composed of a three-dimensional Cartesian mesh with 2.88 million grid blocks simulating an areal extent of 5000 m × 10,000 m × 1800 m (Fig. 1C), and individual grid-block geometry of 25 m × 50 m × 25 m, respectively. Prior to CO_2 injection simulations, steady-state (initial) conditions were computed by imposing (1) a Dirichlet temperature and pressure boundary across the top of the reservoir domain (T = 7 °C, P = 0.101 MPa) to represent atmospheric conditions typical of the eastern Snake River Plain, (2) a Neuman heat boundary (0.11 W m^{-2}) across the bottom of the domain to account for the regional geothermal flux known to exist within the eastern Snake River Plain (Brott et al., 1981), and (3) adiabatic temperature and pressure boundaries elsewhere. These initial conditions represent a fully saturated system from ground surface to 1800 m depth, with linear hydrostatic temperature and pressure profiles ranging from 7 °C to 96 °C and 0.101 MPa to 17.3 MPa, respectively. These initial conditions suggest that CO_2 will exist in the supercritical phase at depths greater than 762.5 m.

CO_2 injections were simulated within each reservoir using TOUGH2-MP (Zhang et al., 2008) with equation of state module ECO2N (Pruess, 2005) for simulating nonisothermal mixtures of water, salt, and CO_2. For simulating CO_2 injections, the upper and lower boundary conditions remained unchanged from the initial conditions simulation; however, the lateral boundary conditions were changed to impose Dirichlet conditions along the vertical edges of each reservoir, thus holding the linear temperature and pressure profiles constant in the far-field regions of the model domain. In order to account for the interaction of two-phase flow (aqueous and supercritical CO_2), the permeability of each phase was modeled using generic characteristic curves. The van Genuchten (1980) relative permeability model was applied for the gas phase in the flow interiors and for the aqueous phase in both flow interior and rubble zone subdomains, while the Corey (1954) relative permeability model was used for the gas phase in the rubble zone subdomain (Table 3). In addition, the capillary pressure effects between the aqueous phase and nonwetting supercritical CO_2 phase were modeled using the commonly invoked van Genuchten (1980) capillary pressure curves (Table 3). The injection well was simulated in each reservoir as a single grid block centered in the horizontal plane at a depth of 1562.5 m, and CO_2 was injected at a constant mass rate of 21.6 kg s^{-1} (680,000 metric tons per year) and formation temperature of 84.5 °C.

ANALYSIS AND DISCUSSION

One of the primary concerns in pursuing large-scale CCS projects is that increasing pore-fluid pressure may induce or trigger seismic activity, the result of which threatens reservoir integrity for CO_2 trapping (Zoback and Gorelick, 2012). In response to this concern, much emphasis has been placed on evaluating the geomechanical changes within target CCS reservoirs. For example, Lucier et al. (2006) and Goodarzi et al. (2011) used separate and coupled, respectively, hydromechanical models to show that small fluid pressure increases during CO_2 injections may induce shear failure in the cap rock seal overlying the Rose Run Sandstone formation in southeast Ohio. Although CCS operations in basalt reservoirs are predicated largely on rapid mineralization rates, rather than low-permeability cap rock seals, these results highlight the importance of understanding how increasing pore-fluid pressures influence reservoir geomechanics.

Tensile Failure

In low-volume basalt reservoirs, vertical fluid flow is suppressed by the presence of relatively low-permeability basalt-flow interiors. These flow interiors are characterized by a central entablature zone consisting of tightly welded fractures with highly variable orientations (Schaefer and Kattenhorn, 2004). The entablature forms during basalt-flow emplacement as the upper and lower cooling fronts meet, and the resulting thermal interactions blunt columnar joint propagation through the entablature (Kattenhorn and Schaefer, 2008). In a multiple-phase hydrogeologic system consisting of an

TABLE 3. RELATIVE PERMEABILITY AND CAPILLARY PRESSURE MODEL PARAMETERS

		λ	S_{lr}	S_{ls}	S_{gr}	$1/P_0$	Max. P_{cap}
Flow interior	Rel. perm.	0.75	0.20	0.99	0.01	—	—
	Cap. press.	0.75	0.00	0.99	—	4.80E–5	1.00E+7
Rubble zone	Rel. perm.	0.75	0.30	1.00	0.00	—	—
	Cap. press.	0.75	0.00	0.99	—	1.38E–3	1.00E+7

Note: λ —phase interference parameter, also called van Genuchten's m (–)]; S_{lr}—liquid-phase residual saturation (–); S_{ls}—liquid-phase saturated saturation (–); S_{gr}—gas-phase residual saturation (–), when set to 0, the Corey (1954) relative permeability model is invoked; P_0—air entry pressure (Pa); P_{cap}—capillary pressure (Pa).

aqueous phase and nonwetting supercritical CO_2 phase, the tightly welded entablature fractures also suggest that capillary pressure effects may inhibit vertical CO_2 migration through the basalt pile. As a result, entablature units within basalt-flow interiors are generally considered barriers to fluid migration; however, since the vertical dimension of low-volume basalt flows is relatively small (on the order of meters to tens of meters), the efficacy of the entablature zone to inhibit vertical fluid flow may be reduced in response to mode I fracture propagation (opening motion). Moreover, since fluid flux within a fracture roughly increases with the cube of fracture aperture (Witherspoon et al., 1980), fracture propagation through the entablature may drastically increase vertical effective permeability and break down any capillary trapping effects.

Although permanent CO_2 disposal in basalt formations is predicated on mineral trapping (McGrail et al., 2006) rather than physical trapping beneath low-permeability cap rock seals, the feasibility of CO_2 sequestration in these systems is inextricably linked with short-term physical trapping within the basalt pile. As a result, understanding the potential for pressure-induced permeability changes prior to widespread mineralization remains a vital component to assessing the feasibility of sequestration in such systems. To examine the potential for mode I fracture propagation in this model scenario, we simulated time-series pressure data at the CO_2 injection site for each simulation (Fig. 2). Since CO_2 is placed in the system at a constant mass rate (21.6 kg s^{-1}), variability in pressure magnitude and accumulation rate within each simulation are solely a function of the spatial distribution of formation heterogeneity, and this suggests that interconnectivity of permeable structures (i.e., interconnected upper colonnades and rubbly flow margins) away from the injection site into the target reservoir can substantially reduce injection pressure. Conversely, injection pressure accumulates when high-permeability structures near the injection well become disconnected from the far field of the reservoir (Pollyea and Fairley, 2012). The effects of this injection pressure with respect to mode I fracture propagation can be evaluated by estimating the pressure required to induce hydraulic fracture at depth, which, for this analysis, was computed using the method proposed by Eaton (1969):

$$F = \left[\frac{\sigma_{\text{lith}}}{D} - \frac{P_{\text{f}}}{D}\right]\left(\frac{\nu}{1-\nu}\right) + \frac{P_{\text{f}}}{D}, \qquad (1)$$

where F is the fracture gradient, σ_{lith} is the lithostatic stress, P_{f} is pore-fluid pressure, ν is Poisson's ratio, and D is depth. Using D = 1562.5 m (the midpoint of the injection block) and a Poisson's ratio of 0.25, the estimated fracture gradient is 0.0152 MPa m^{-1} (0.67 psi ft^{-1}), which results in a fracture pressure of 23.7 MPa at injection depth (Fig. 2, dashed line). Results from the 50 simulations indicate that 4% (2/50) of the simulations exceed the fracture pressure near the injection site (Fig. 2). Although this result is promising, it must be noted that in the two cases in which there was failure, injection pressures exceeded the fracture gradient by >2 MPa, suggesting that fracture propagation through low-permeability entablature units may be widespread in these cases. In light of the costs associated with developing a CCS reservoir, the practical implication of this result is that formation injectivity cannot be assumed to be favorable in low-volume basalt formations. As a result, reservoir characterization and well siting must quantify both near-well fracture heterogeneity and connectivity into the target reservoir in order to minimize the risk of mode I fracture propagation and the associated permeability increases that may result.

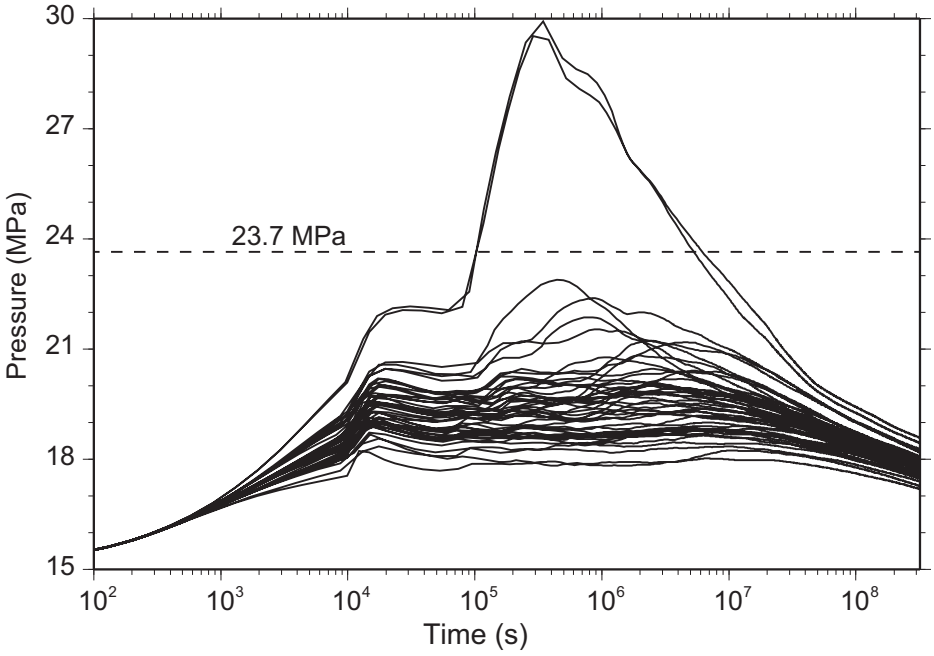

Figure 2. Solid lines represent time-series pressure at the injection site for 50 CO_2 injection simulations. The dashed line denotes pressure required for mode I failure estimated using the Eaton (1969) method.

Shear Failure

The eastern Snake River Plain in southern Idaho is located along the northeast margin of the Basin and Range Province, and it is generally considered an extensional tectonic environment (Geslin et al., 2002; Payne et al., 2008), although it has been suggested that stresses within the eastern Snake River Plain may be isotropic (Moos et al., 1990). In evaluating the likelihood of shear failure for optimally aligned faults/fractures in response to industrial-scale CO_2 injections, this work assumes an extensional stress regime, such that $S_h \leq S_H < S_V$, where S_h and S_H are the minimum and maximum horizontal compressive stresses, respectively, and S_V is lithostatic stress. One limitation to this analysis is that a detailed literature review reveals that little is known about the magnitudes of horizontal compressive stresses within the eastern Snake River Plain. As a result, this work considers three possibilities for minimum horizontal compressive stress in the target reservoir: (1) $S_h = 0.85S_V$, (2) $S_h = 0.70S_V$, and (3) $S_h = 0.55S_V$.

To account for the presence of pore-fluid pressure (P_f), the static (prior to CO_2 injection) vertical effective stress ($S_{V,eff}$) is computed as a function of depth using the relationship:

$$S_{\text{V,eff}}(z) = \left(\rho_{\text{r}} - \rho_{\text{f}}\right) g z, \qquad (2)$$

where ρ_r is the reservoir rock density, ρ_f is the aqueous-phase fluid density, g is acceleration due to gravity, and z is depth within the reservoir (Fig. 3, black line). The effects of increasing pore-fluid pressures that result from the CO_2 injections are accounted for using simulated

grid-block pressures. In particular, the mean injection pressure, $\overline{P}_{f(x,y,z)}$, for each grid block for all 50 simulations is computed as:

$$\overline{P}_{f(x,y,z)} = \frac{1}{50}\sum_{i=1}^{50} P_{f,i(x,y,z)}, \quad (3)$$

where $P_{f(x,y,z)}$ is the modeled injection pressure at location (x,y,z) within the model domain for simulation i. This injection pressure acts in opposition to all compressive stresses within the target reservoir; however, we are primarily interested in whether the injection pressures move $S_{h,eff}$ below the Mohr-Coulomb failure threshold. Here, we invoke the Mohr-Coulomb failure criteria for an extensional stress regime in terms of the minimum and maximum principal stresses:

$$\sigma_{3,eff} = \sigma_{1,eff}\left[\left(\mu_s + 1\right)^{1/2} + \mu_s\right]^{-2}, \quad (4)$$

where $\sigma_{3,eff}$ is the value of $S_{h,eff}$ below which shear failure is possible for optimally aligned faults or fractures, $\sigma_{1,eff}$ is the vertical compressive effective stress ($S_{V,eff}$), and μ_s is the coefficient of static friction (Engelder, 1993). For the coefficient of static friction, we assume a value of 0.85 on the basis of Byerlee (1978, p. 624). Since injection pressures are variable within each CO_2 injection simulation as function of time (t), the mean minimum compressive effective stress, $\overline{S}_{h,eff}(t)$, is computed as:

$$\overline{S}_{h,eff}(t) = S_h - \overline{P}_{f(x,y,z)}(t), \quad (5)$$

where S_h is the minimum horizontal stress, and $\overline{P}_{f(x,y,z)}(t)$ is mean grid-block injection pressure for the time step (t) computed per Equation 3. After 30 d of constant-rate CO_2 injections, this model suggests that optimally oriented fractures may fail in response to injection pressure if $S_h \approx 0.55S_V$. As shown in Figure 3 (blue circles), the vertical length scale for shear failure in this scenario is ~150 m from the injection site; however, this length is conservative because the horizontal semivariogram correlation range for high-permeability units is an order of magnitude longer than in the vertical direction. In addition, for $S_h \approx 0.70S_V$, shear failure is possible within bounds of uncertainty equivalent to three standard deviations from the $\overline{S}_{h,eff}$ (Fig. 3, green error bars). Because the model variability is solely a function of the spatial distribution of reservoir heterogeneity, these results suggest that (1) more complete information is needed with respect to the in situ stresses within the eastern Snake River Plain, and (2) understanding the orientation of fractures in close proximity to the injection well is an important criteria for both understanding risks associated with induced or triggered seismicity and evaluating the likelihood of damaging transport-inhibiting basalt-flow interiors through shear failure.

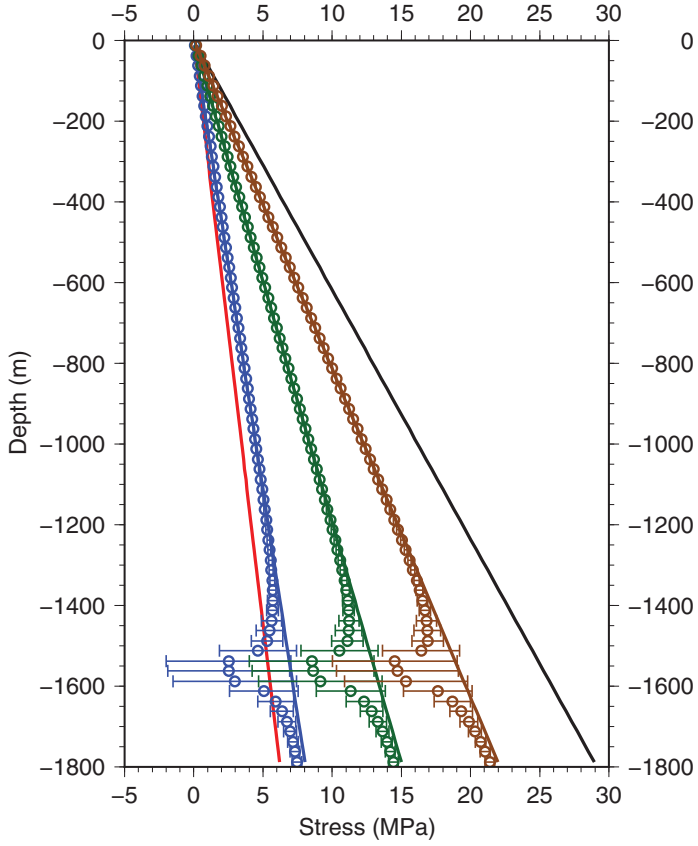

Figure 3. Minimum and maximum principal stresses as a function of depth for an extensional stress regime. The solid black line denotes the maximum compressive effective stress ($S_{V,eff}$), which is vertical in an extensional stress regime. Three scenarios are considered for the minimum compressive effective stress ($S_{h,eff}$) within the domain: $S_{h,eff} = 0.85S_{V,eff}$ (brown); $S_{h,eff} = 0.70S_{V,eff}$ (green); $S_{h,eff} = 0.55S_{V,eff}$ (blue). For each scenario, the stress profile is computed at 30 d of constant-rate CO_2 injection using a vertical column of model grid cells that intersect the injection well. Solid lines denote the minimum compressive effective stress prior to CO_2 injections, circles denote mean (N = 50) $S_{h,eff}$ for each grid cell (Eq. 5), and error bars represent bounds of uncertainty corresponding to three standard deviations (3σ) from the mean 30 d $S_{h,eff}$. The red line is Mohr-Coulomb failure criteria as a function of depth (Eq. 4).

CO_2 Transport and Confinement

In the absence of low-permeability cap rock to physically trap injected CO_2 within the target reservoir, the feasibility of CCS in basalt formations will largely depend on carbonate mineralization to permanently isolate CO_2 from the atmosphere. This suggests that physical CO_2 confinement in early time, i.e., prior to widespread mineralization, will be necessary to allow such geochemical interactions to commence. Although fully coupled thermal-hydro-mechanical models capable of approximating water-CO_2-basalt mineralization reactions are beyond the capabilities of current simulation codes (Fairley et al., 2010), we can use the present simulations to estimate the probability of CO_2 confinement for low-volume basalt reservoirs in the absence of mineralization, i.e., a worst-case scenario. In the numerical model presented here, 13.6 million metric tons of CO_2 are placed into the system after 20 yr of constant-rate (21.6 kg s^{-1}) injection. Of this CO_2 mass, the mean (N = 50) phase partition consists of 9.7 million metric tons (71%) in the supercritical phase and 3.9 million metric tons

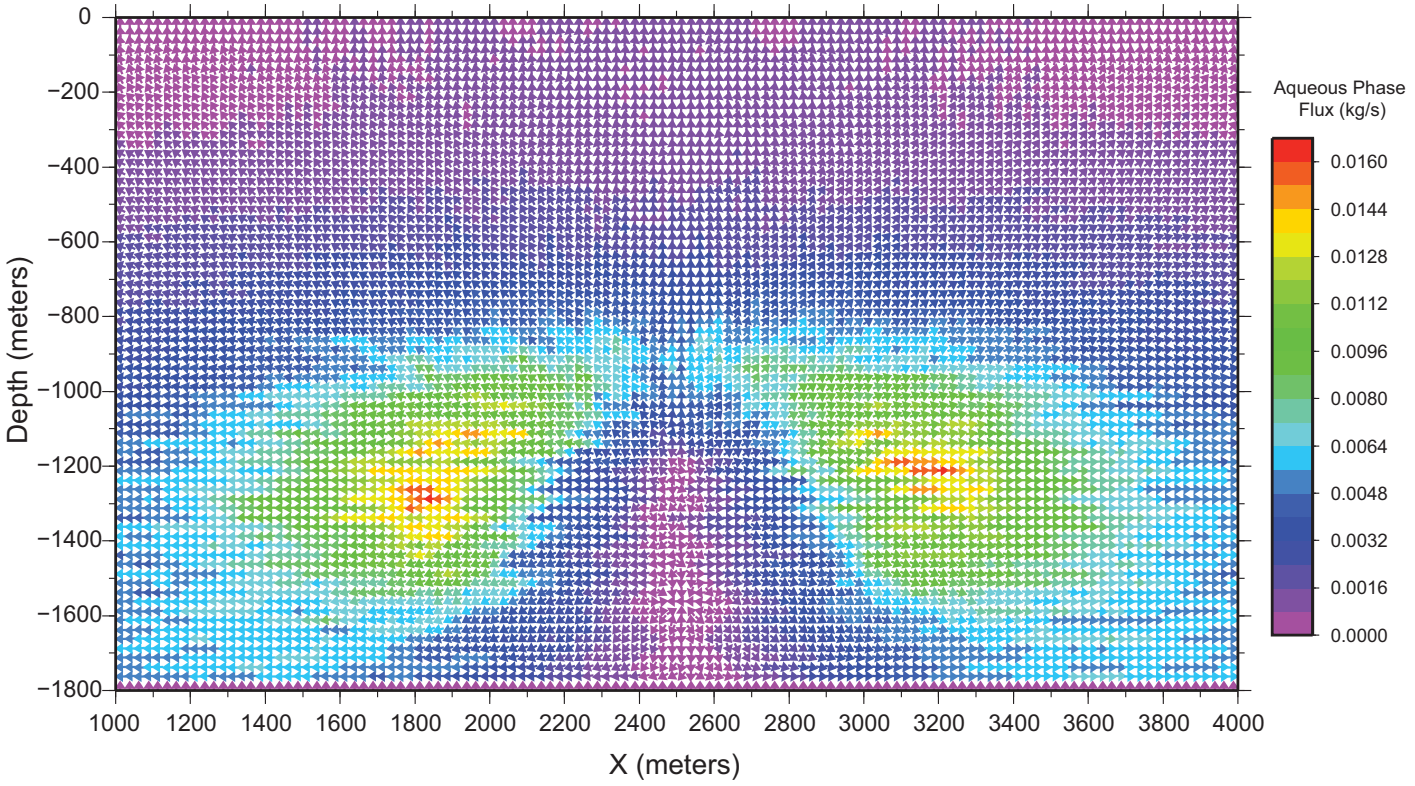

Figure 4. Mean (N = 50) aqueous-phase mass flux (kg s^{-1}) vectors in the x-z plane through the injection site; arrows denote flux direction, and color palette denotes flux magnitude.

(29%) dissolved in the aqueous phase. Due to the density differential between the CO_2-rich aqueous phase and natural formation water, the CO_2-rich aqueous phase sinks under gravity-driven flow (Fig. 4), suggesting that solubility trapping is a significant contributor to CO_2 isolation in the fractured basalt reservoirs. Nevertheless, a substantial quantity of CO_2 remains in the supercritical phase, which is buoyant with respect to both natural formation water and the CO_2-rich aqueous phase. The mean supercritical-phase flux after 20 yr of injection indicates that vertical mass transport is less than 5.0×10^{-4} kg s^{-1} above 750 m depth, which is marginally above the critical point for CO_2 (Fig. 5A). In addition, the uncertainty associated with this estimate is less than 1.0×10^{-4} normalized variance (Fig. 5B). As a result, the overall physical confinement potential of low-volume basalts is promising over a time scale of 20 yr; however, these results must be qualified because several important physical processes are not described in the simulation code deployed for this work. In particular, the effects of mineralization/dissolution reactions, including reservoir permeability changes and the force of crystallization, may adversely affect reservoir performance; however, equations of state that fully describe these processes are a well-known and unsolved challenge for developing fully coupled thermal-hydromechanical models (Fairley et al., 2010) at the time of writing.

CONCLUSIONS

In this work, we investigated geologic carbon sequestration in low-volume basalt formations typical of the eastern Snake River Plain in southern Idaho, USA. This investigation builds on the previous work of Pollyea and Fairley (2012) by developing a three-dimensional Monte Carlo flow and transport model whereby model variability is solely a function of spatially distributed formation heterogeneity, which is a priori unknown within the eastern Snake River Plain at depths of interest for geologic carbon sequestration. This approach, although not specific to any one site within the eastern Snake River Plain, benefits from the ability to quantify a wide range of system behaviors that result from the inherent uncertainty. Fifty identically parameterized CO_2 injection simulations were computed using equally probable synthetic reservoirs constrained on the basis of an anisotropic semivariogram model that describes the characteristic spatial dependence of high-permeability structures within a basalt pile.

The results of this model indicate that low-volume basalt reservoirs exhibit sufficient confinement potential over a 20 yr CO_2 injection program to accommodate mineral trapping rates suggested in the literature (McGrail et al., 2006; Schaef et al., 2011). In addition, geomechanical analysis of time-series pressure accumulation at the injection site indicates that the potential for tensile failure is low; however, the implications of such failure may drastically reduce the confinement potential by propagating preexisting columnar joints through low-permeability entablature zones within basalt-flow interiors. Interpreting the potential for shear failure in response to injection is less conclusive because a detailed literature review indicates that little is known about the magnitudes of in situ principal stresses with the eastern Snake River Plain, although it is generally assumed to be an extensional stress regime. Nevertheless, we evaluate the Mohr-Coulomb shear failure criteria using three scenarios for an extensional stress regime: $S_h = 0.85S_V$, $S_h = 0.70S_V$, and $S_h = 0.55S_V$. This analysis indicates that the mean (N = 50) injection pressure after 30 d of injection may induce or trigger shear failure for optimally oriented fractures within the reservoir for $S_h = 0.55S_V$. In contrast, the mean injection pressure for $S_h = 0.70S_V$ results in a

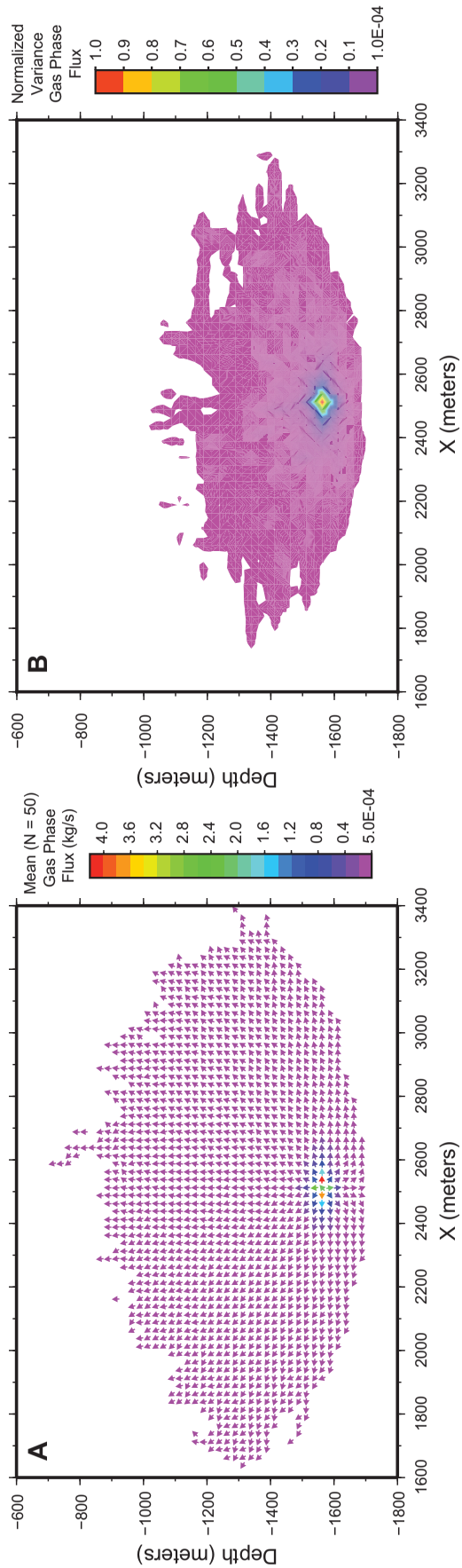

Figure 5. (A) Mean (N = 50) supercritical-phase mass flux (kg s^{-1}) in the x-z plane through the injection site; arrows denote flux direction, and color palette denotes flux magnitude for values greater than 5.0 × 10^{-4} kg s^{-1}. (B) Normalized variance of supercritical-phase mass flux for 50 simulations; note that values less than 1.0 × 10^{-4} are not shown.

minimum effective horizontal stress above the Mohr-Coulomb failure criteria; however, failure is possible for this scenario within the bounds of uncertainty, corresponding to three standard deviations from the mean injection pressure.

ACKNOWLEDGMENTS

We thank Clare Bond, Julia Eve Hammer (*Geological Society of America Bulletin* associate editor), and one anonymous reviewer for their thoughtful comments and suggestions for improvements on this manuscript. This work received financial support from the Center for Advanced Energy Studies under contract number DE-AC07-051D14517.

REFERENCES CITED

Alexander, G., Maroto-Valer, M.M., and Gafarova-Aksoy, P., 2007, Evaluation of reaction variables in the dissolution of serpentine for mineral carbonation: Fuel, v. 86, p. 273–281, doi:10.1016/j.fuel.2006.04.034.

Brott, C.A., Blackwell, D.D., and Ziagos, J.P., 1981, Thermal and tectonic implications of heat flow in the eastern Snake River Plain, Idaho: Journal of Geophysical Research, v. 86, p. 11,709–11,734, doi:10.1029/JB086iB12p11709.

Byerlee, J., 1978, Friction of rocks: Pure and Applied Geophysics, v. 116, p. 615–626, doi:10.1007/BF00876528.

Corey, A., 1954, The interrelation between gas and oil relative permeabilities: Producers Monthly, v. 19, p. 38–41.

Deutsch, C.V., 2002, Geostatistical Reservoir Modeling: New York, Oxford University Press, 384 p.

Eaton, B.A., 1969, Fracture gradient prediction and its application in oilfield operations: Journal of Petroleum Technology, v. 21, p. 1353–1360, doi:10.2118/2163-PA.

Engelder, T., 1993, Stress Regimes in the Lithosphere: Princeton, New Jersey, Princeton University Press, 451 p.

Fairley, J., Ingebritsen, S., and Podgorney, R., 2010, Challenges for numerical modeling of enhanced geothermal systems: Ground Water, v. 48, p. 482–483, doi:10.1111/j.1745-6584.2010.00716.x.

Geslin, J.K., Link, P.K., Riesterer, J.W., Kuntz, M.A., and Fanning, C.M., 2002, Pliocene and Quaternary stratigraphic architecture and drainage systems of the Big Lost Trough, northeastern Snake River Plain, Idaho, *in* Link, P.K., and Mink, L., eds., Geology, Hydrogeology, and Environmental Remediation: Idaho National Engineering and Environmental Laboratory, Eastern Snake River Plain, Idaho: Geological Society of America Special Paper 353, p. 11–26.

Goldberg, D.S., Takahashi, T., and Slagle, A.L., 2008, Carbon dioxide sequestration in deep-sea basalt: Proceedings of the National Academy of Sciences of the United States of America, v. 105, p. 9920–9925, doi:10.1073/pnas.0804397105.

Goldberg, D.S., Kent, D.V., and Olsen, P.E., 2010, Potential onshore and offshore reservoirs for CO_2 sequestration in Central Atlantic magmatic province basalts: Proceedings of the National Academy of Sciences of the United States of America, v. 107, p. 1327–1332, doi:10.1073/pnas.0913721107.

Goodarzi, S., Settari, A., Zoback, M., and Keith, D., 2011, A coupled geomechanical reservoir simulation analysis of carbon dioxide storage in a saline aquifer in the Ohio River Valley: Environmental Geoscience, v. 18, p. 189–207, doi:10.1306/eg.04061111002.

International Energy Agency (IEA), 2013, World Energy Outlook Special Report 2013: Redrawing the Energy Climate Map: Paris, France, International Energy Agency, 10 June 2013, http://www.iea.org/publications/freepublications/publication/WEO_RedrawingEnergyClimateMap.pdf (accessed 28 June 2013).

Jayaraman, K., 2007, India's carbon dioxide trap: Nature, v. 445, p. 350, doi:10.1038/445350a.

Kattenhorn, S.A., and Schaefer, C.J., 2008, Thermal-mechanical modeling of cooling history and fracture development in inflationary basalt lava flow: Journal of

Volcanology and Geothermal Research, v. 170, p. 181–197, doi:10.1016/j.jvolgeores.2007.10.002.

Kelley, D.S., Karson, J.A., Blackman, D.K., Fruh-Green, G.L., Butterfield, D.A., Lilley, M.D., Olson, E.J., Schrenk, M.O., Roe, K.K., Lebon, G.T., and Rivizzingo, P., 2001, An off-axis hydrothermal vent field near the Mid-Atlantic Ridge at 30°N: Nature, v. 412, p. 145–149, doi:10.1038/35084000.

Lucier, A., Zoback, M., Gupta, N., and Ramakrishnan, T., 2006, Geomechanical aspects of CO_2 sequestration in a deep saline reservoir in the Ohio River Valley region: Environmental Geoscience, v. 13, p. 85–103, doi:10.1306/eg.11230505010.

Matter, J.M., and Kelemen, P.B., 2009, Permanent storage of carbon dioxide in geological reservoirs by mineral carbonation: Nature Geoscience, v. 2, p. 837–841, doi:10.1038/ngeo683.

McGrail, B.P., Schaef, H.T., Ho, A.M., Chien, Y.-J., and Dooley, J.J., 2006, Potential for carbon dioxide sequestration in flood basalts: Journal of Geophysical Research, v. 111, B12201, doi:10.1029/2005JB004169.

Moos, D., Barton, C., and Smith, R., 1990, Results of borehole televiewer logging to 3km in the Snake River Plain—In situ stress and fractures: Washington, D.C., American Geophysical Union, Fall Meeting, Abstracts, v. 71, p. 1622, doi:10.1029/E0071i043p01219.

Orr, F.M., Jr., 2009, Perspective: Onshore geologic storage of CO_2: Science, v. 325, p. 1656–1658, doi:10.1126/science.1175677.

Pacala, S., and Socolow, R., 2004, Stabilization wedges: Solving the climate problem for the next 50 years with current technologies: Science, v. 305, p. 968–972, doi:10.1126/science.1100103.

Payne, S.J., McCaffrey, R., and King, R.W., 2008, Strain rates and contemporary deformation in the Snake River Plain and surrounding Basin and Range from GPS and seismicity: Geology, v. 36, p. 647–650, doi:10.1130/G25039A.1.

Pollyea, R.M., and Fairley, J.P., 2011, Estimating surface roughness of terrestrial laser scan data using orthogonal distance regression: Geology, v. 39, p. 623–626, doi:10.1130/G32078.1.

Pollyea, R.M., and Fairley, J.P., 2012, Implications of spatial reservoir uncertainty for CO_2 sequestration in the East Snake River Plain, Idaho (USA): Hydrogeology Journal, v. 20, p. 689–699, doi:10.1007/s10040-012-0847-1.

Pruess, K., 2005, ECO2N: A TOUGH2 Fluid Property Module for Mixtures of Water, NaCl, and CO_2: Lawrence Berkeley National Laboratory Technical Report LBNL-57952.

Schaef, H., McGrail, B., and Owen, A., 2011, Basalt reactivity variability with reservoir depth in supercritical CO_2 and aqueous phases: Energy Procedia, v. 4, p. 4977–4984, doi:10.1016/j.egypro.2011.02.468.

Schaefer, C.J., and Kattenhorn, S.A., 2004, Characterization and evolution of fractures in low-volume pahoehoe lava flows, eastern Snake River Plain, Idaho: Geological Society of America Bulletin, v. 116, p. 322–336, doi:10.1130/B25335.1.

van Genuchten, M., 1980, A closed-form equation for predicting the hydraulic conductivity of unsaturated soils: Soil Science Society of America, v. 44, p. 892–898, doi:10.2136/sssaj1980.03615995004400050002x.

Welhan, J., Smith, R., and Wylie, A., 1997, Stochastic modeling of hydraulic conductivity in the Snake River Plain aquifer: 1. Hydrogeologic constraints and conceptual approach, *in* Sharma, S., and Hardcastle, J.H., eds., Proceedings of the 32nd Symposium on Engineering Geology and Geotechnical Engineering: Pocatello, Idaho, College of Engineering, Idaho State University, p. 75–91.

Welhan, J.A., Clemo, T.M., and Gégo, E.L., 2002a, Stochastic simulation of aquifer heterogeneity in a layered basalt aquifer system, eastern Snake River Plain, Idaho, *in* Link, P.K., and Mink, L., eds., Geology, Hydrogeology, and Environmental Remediation: Idaho National Engineering and Environmental Laboratory, Eastern Snake River Plain, Idaho: Geological Society of America Special Paper 353, p. 225–247.

Welhan, J.A., Johannesen, C.A., Davis, L.L., Reeves, K.S., and Glover, J.A., 2002b, Overview and synthesis of lithologic controls on aquifer heterogeneity in the eastern Snake River Plain, Idaho, *in* Bonnichsen, B., White, C., and McCurry, M., eds., Tectonic and Magmatic Evolution of the Snake River Plain Volcanic Province: Idaho Geological Survey Bulletin 30, p. 455–460.

Welhan, J.A., Johannesen, C.M., Reeves, K.S., Clemo, T.M., Glover, J.A., and Bosworth, K.W., 2002c, Morphology of inflated pahoehoe lavas and spatial architecture of their porous permeable zones, eastern Snake River Plain, Idaho, *in* Link, P.K., and Mink, L., eds., Geology, Hydrogeology, and Environmental Remediation: Idaho National Engineering and Environmental Laboratory, Eastern Snake River Plain, Idaho: Geological Society of America Special Paper 353, p. 135–150.

Witherspoon, P., Wang, J., Iwai, K., and Gale, J., 1980, Validity of cubic law for fluid flow in a deformable rock fracture: Water Resources Research, v. 16, p. 1016–1024, doi:10.1029/WR016i006p01016.

Zhang, K., Wu, Y.-S., and Pruess, K., 2008, User's Guide for TOUGH2-MP—A Massively Parallel Version of the TOUGH2 Code: Lawrence Berkeley National Laboratory Technical Report LBNL-315E, 108 p.

Zoback, M., and Gorelick, S.M., 2012, Earthquake triggering and large-scale geologic storage of carbon dioxide: Proceedings of the National Academy of Sciences of the United States of America, v. 109, p. 10,164–10,168, doi:10.1073/pnas.1202473109.

Science Editor: A. Hope Jahren
Associate Editor: Julia Eve Hammer

Manuscript Received 17 February 2013
Revised Manuscript Received 19 July 2013
Manuscript Accepted 15 November 2013

Printed in the USA